

Supporting information

Real world luminescence thermometry through novel mixed-metal Eu/Tb complex with furan-containing 1,3-diketone

Trofim A. Polikovskiy¹, Victoria E. Gontcharenko^{1,2}, Anna A. Ivanova³, Darya A. Metlina¹, Mikhail A. Kiskin⁴, Ilya V. Taydakov¹ and Yury A. Belousov^{1,2,3*}

1. *P. N. Lebedev Physical Institute of the Russian Academy of Sciences, 53 Leninskiy I. Prospect, Moscow, 119991, Russia*
2. *Faculty of Chemistry, National Research University Higher School of Economics, 20 Miasnitskaya Str., 101000 Moscow, Russia*
3. *Chemistry Department, Moscow State University, Leninskie Gory, Moscow, 119991, Russia;*
4. *Kurnakov Institute of General and Inorganic Chemistry, Russian Academy of Sciences, Moscow, 119991, Russia*

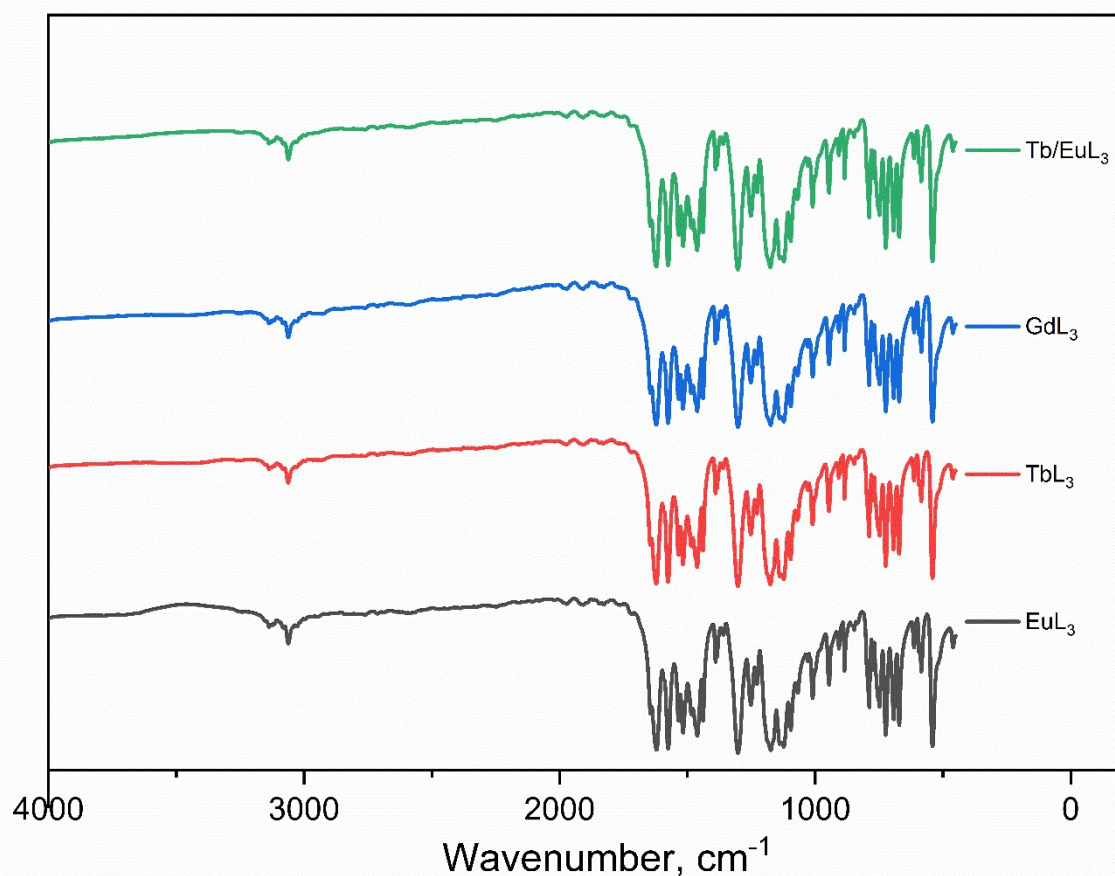


Figure S1. IR spectra of all complexes.

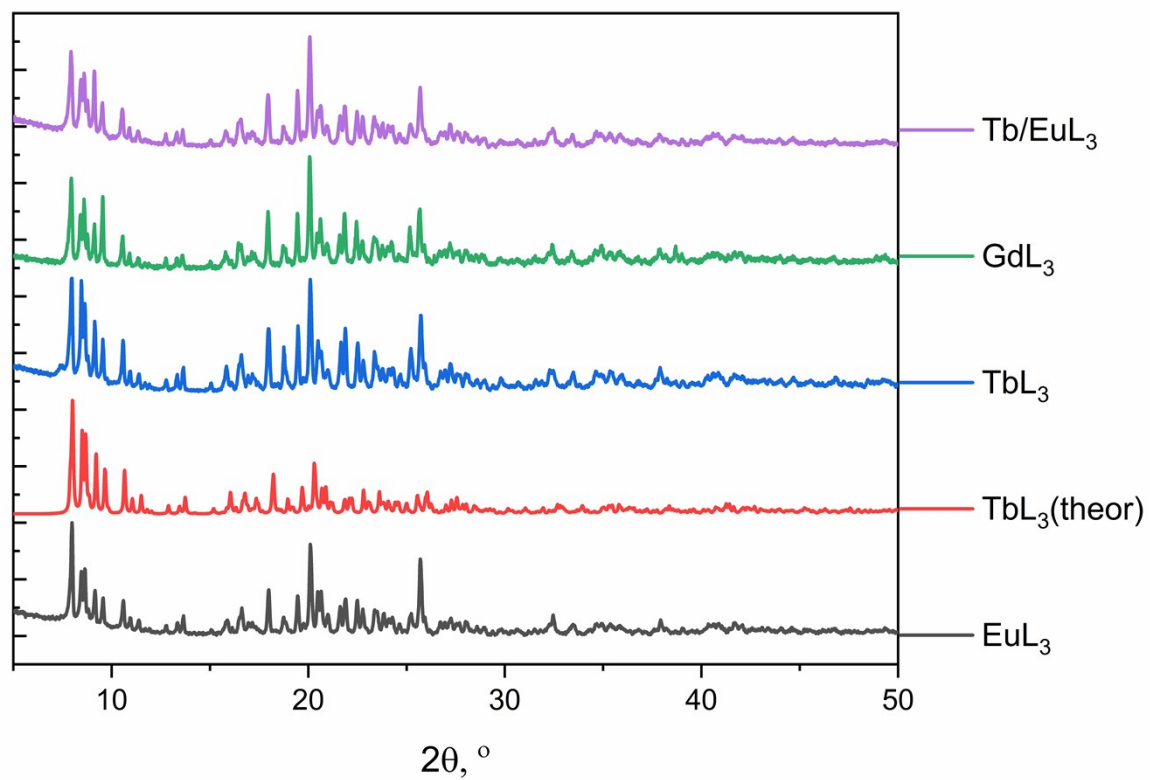


Figure S2. PXRD patterns of all complexes and simulated from single-crystal data of TbL₃.

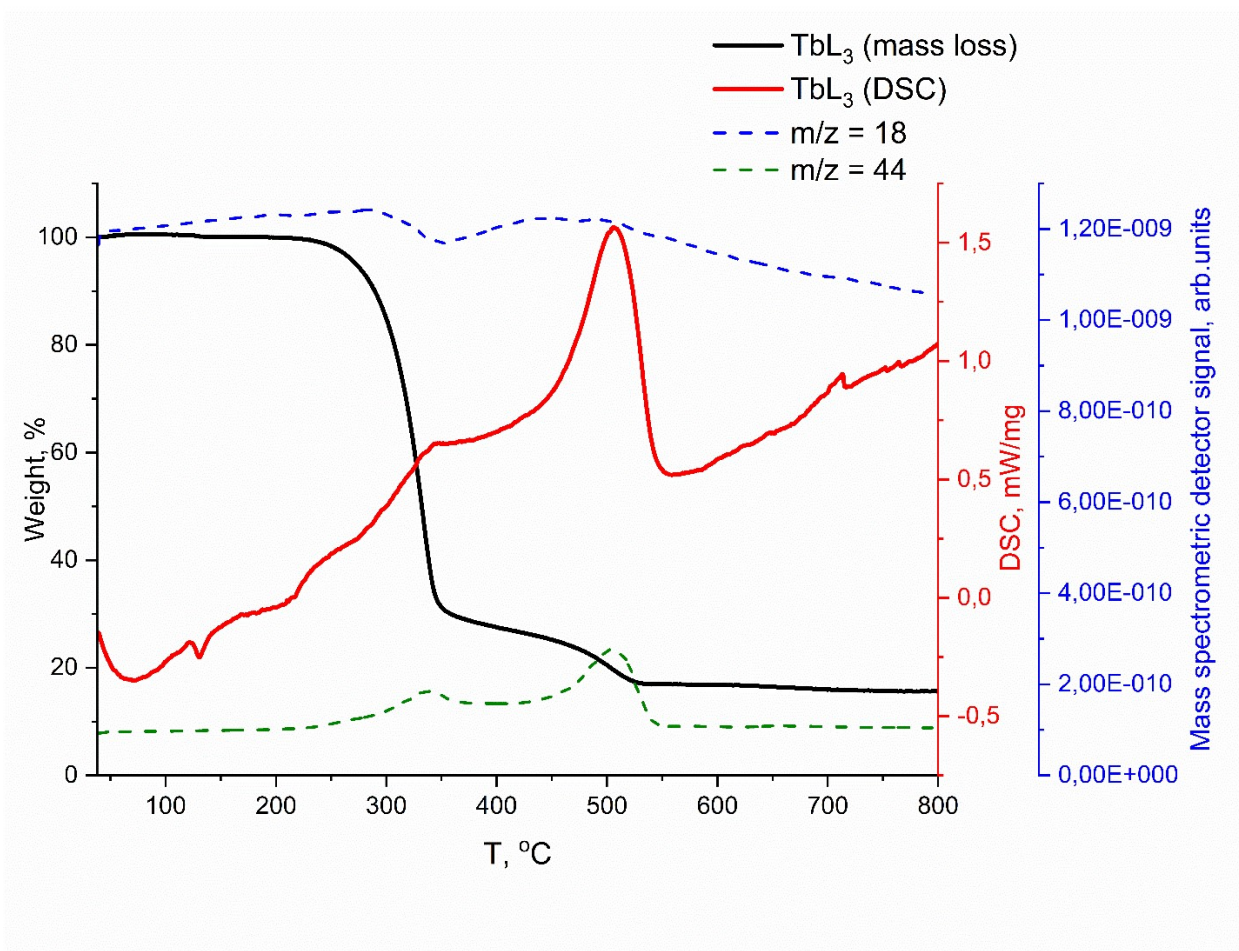


Figure S3. Mass loss curves (TG), DTA, as well as signals from the mass spectrometric detector of thermal decomposition products for complex TbL_3 .

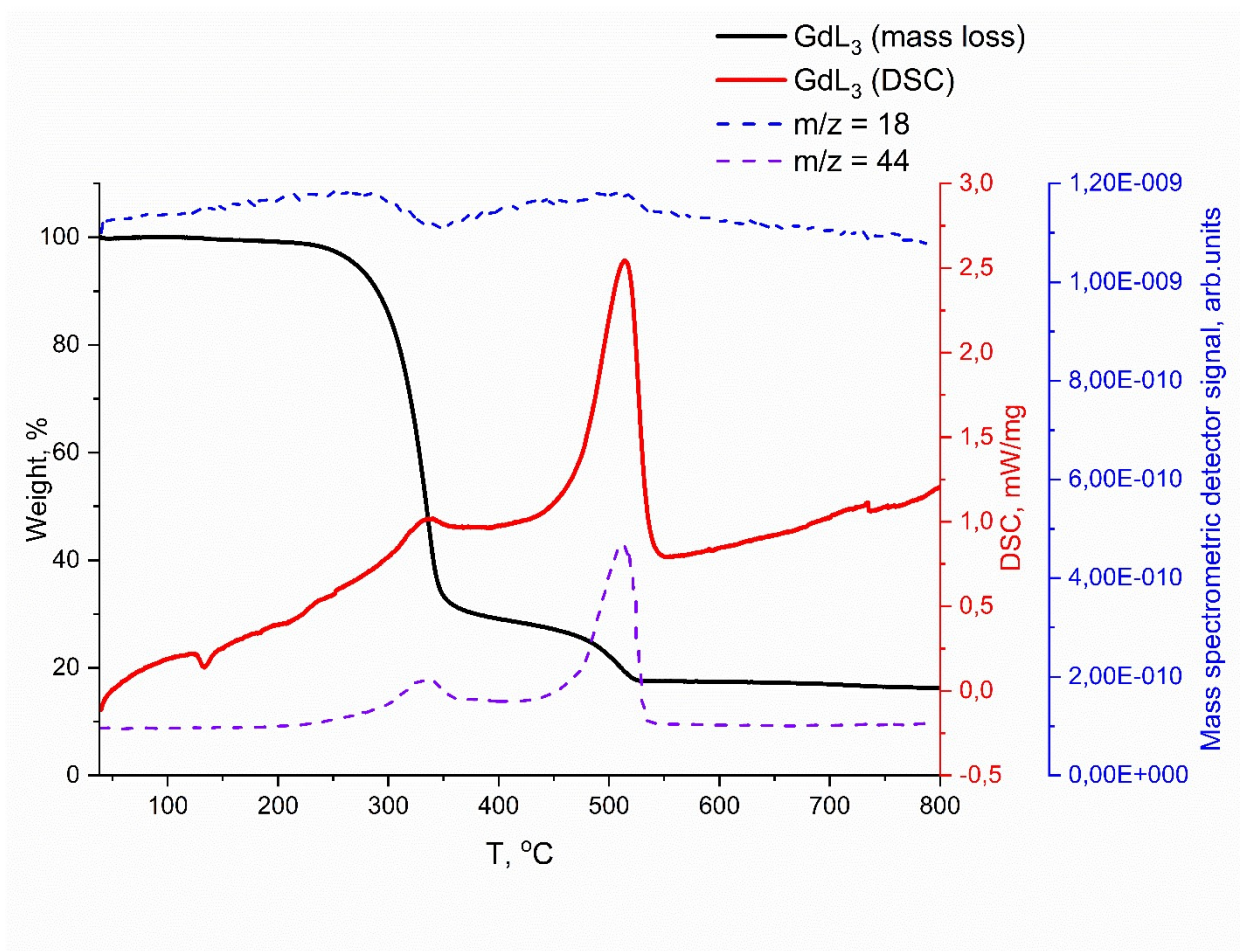


Figure S4. Mass loss curves (TG), DTA, as well as signals from the mass spectrometric detector of thermal decomposition products for complex GdL_3 .

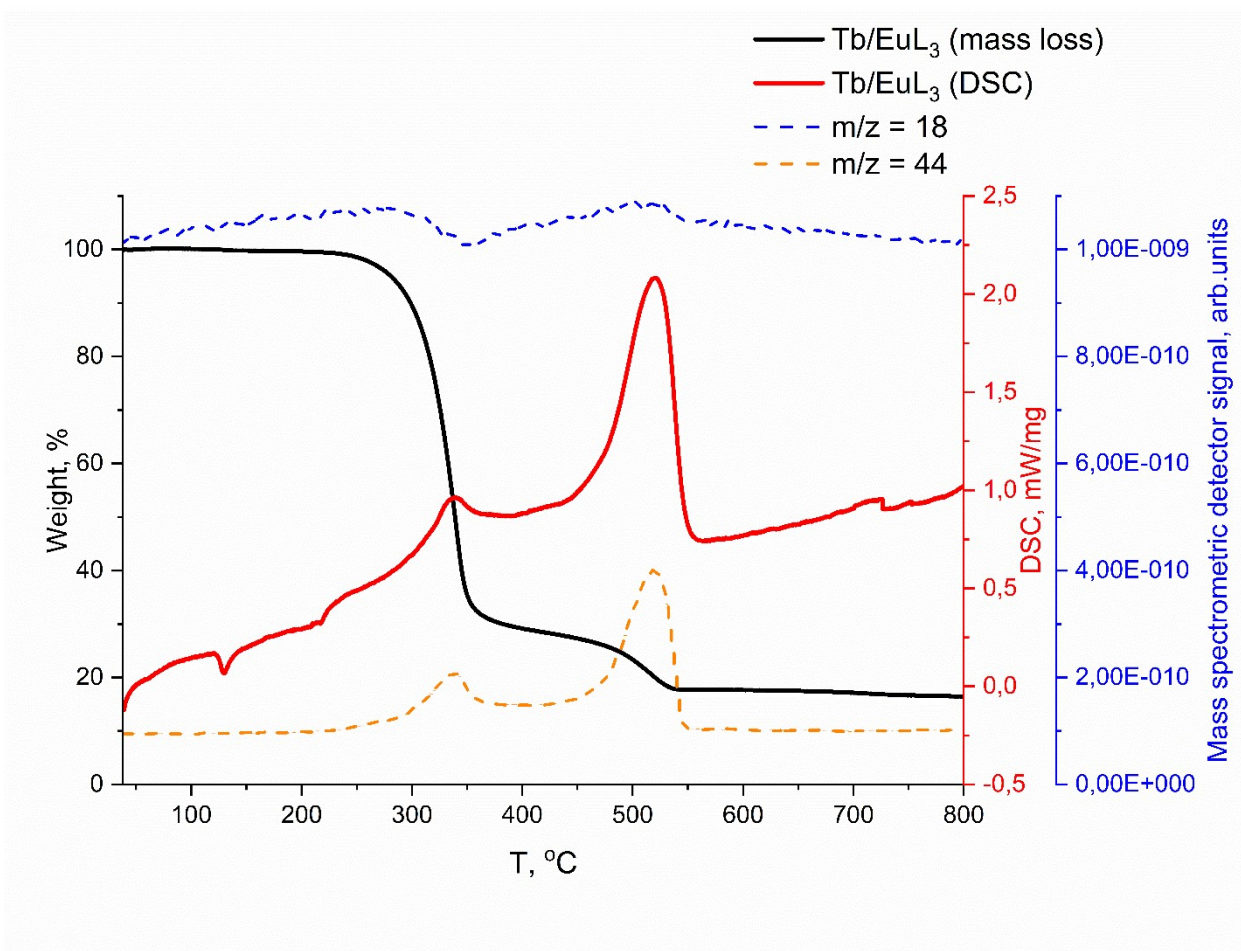


Figure S5. Mass loss curves (TG), DTA, as well as signals from the mass spectrometric detector of thermal decomposition products for complex Tb/EuL₃.

Table S1. Main crystallographic details and refinement parameters for structures **EuL₃**, **GdL₃**, and **TbL₃**.

Compound	EuL₃	GdL₃	TbL₃
CCDC	2357262	2357263	2357261
Empirical formula	C ₆₀ H ₄₂ F ₉ O ₁₁ P ₂ Eu	C ₆₀ H ₄₂ F ₉ O ₁₁ P ₂ Gd	C ₆₀ H ₄₂ F ₉ O ₁₁ P ₂ Tb
Formula weight (g·mol ⁻¹)	1323.83	1329.12	1330.79
T (K)	296(2)	296(2)	100(2)
Crystal system	Triclinic	Triclinic	Triclinic
Space group	P-1	P-1	P-1
a (Å)	10.9872(6)	11.0181(6)	10.9568(3)
b (Å)	11.9498(7)	11.9586(6)	11.8761(3)
c (Å)	22.8307(13)	22.8961(12)	22.7730(7)
α (deg)	80.381(2)	80.485(2)	80.4570(10)
β (deg)	76.839(2)	76.757(2)	76.7030(10)
γ (deg)	70.971(2)	70.868(2)	70.9410(10)
V (Å ³)	2745.2(3)	2761.0(3)	2712.51(13)
Z	2	2	2
D _{calc} (g·cm ⁻³)	1.602	1.599	1.629
θ _{min} -θ _{max} (deg)	2.11-33.32	1.99-33.34	1.85-29.00
μ (mm ⁻¹)	1.294	1.351	1.457
T _{min} /T _{max}	0.5897/0.7466	0.6340/0.7466	0.5184/0.6478
Reflections/Reflection unique number	57556/18880	57535/19701	27410/ 14286
Reflections with I > 2σ(I)	15589	15858	11535
R _{int}	0.0539	0.0456	0.0536
GooF	1.090	1.054	1.028
R ₁ , wR ₂ (I > 2σ(I))	0.0443, 0.0738	0.0435, 0.0712	0.0455, 0.0899
R ₁ , wR ₂ (all data)	0.0635, 0.0843	0.0665, 0.0825	0.0638, 0.0958

Table S2. Ln-O bond lengths in corresponding complexes.

Ln-O bond length, Å	EuL ₃	GdL ₃	TbL ₃
Ln-O1	2.3739(19)	2.3631(18)	2.337(2)
Ln-O2	2.4422(18)	2.4347(18)	2.415(2)
Ln-O4	2.3769(18)	2.3643(18)	2.339(2)
Ln-O5	2.4390(19)	2.4241(18)	2.414(2)
Ln-O7	2.3774(19)	2.3678(18)	2.347(2)
Ln-O8	2.4314(19)	2.4327(18)	2.393(2)
Ln-O10	2.3746(19)	2.3442(18)	2.342(2)
Ln-O11	2.3574(18)	2.3607(18)	2.323(2)

Table S3. Parameters of weak C-H...F intermolecular interactions in corresponding complexes.

Interaction	D-H, Å	H...A, Å	D...A, Å	D-H-A, deg.
EuL₃				
C35-H35...F7 (-1+x, y, z)	0.95	2.41	3.299(4)	161
C42-H42...F9 (1-x, 1-y, 1-z)	0.95	2.49	3.253(4)	139
GdL₃				
C35-H35...F7 (-1+x, y, z)	0.95	2.38	3.295(4)	161
C42-H42...F9 (1-x, 1-y, 1-z)	0.95	2.49	3.258(4)	138
TbL₃				
C35-H35...F7 (-1+x, y, z)	0.95	2.37	3.281(4)	162
C42-H42...F9 (1-x, 1-y, 1-z)	0.95	2.47	3.238(5)	138

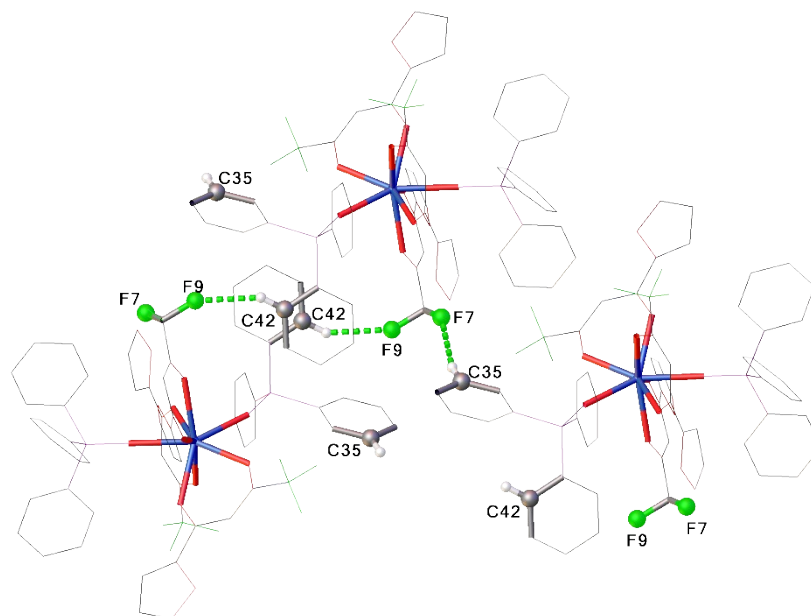


Figure S6. View of C-H...F contacts in TbL₃. Thermal ellipsoids of atomic displacement and hydrogen atoms not involved in intermolecular interactions are omitted for clarity. Atoms involved in intermolecular interactions, as well as Tb³⁺ coordination environment, are highlighted. C-H...F interactions are shown with dashed lines. Molecules correspond to symmetry codes 1-x, 1-y, 1-z; 1+x, y, z.

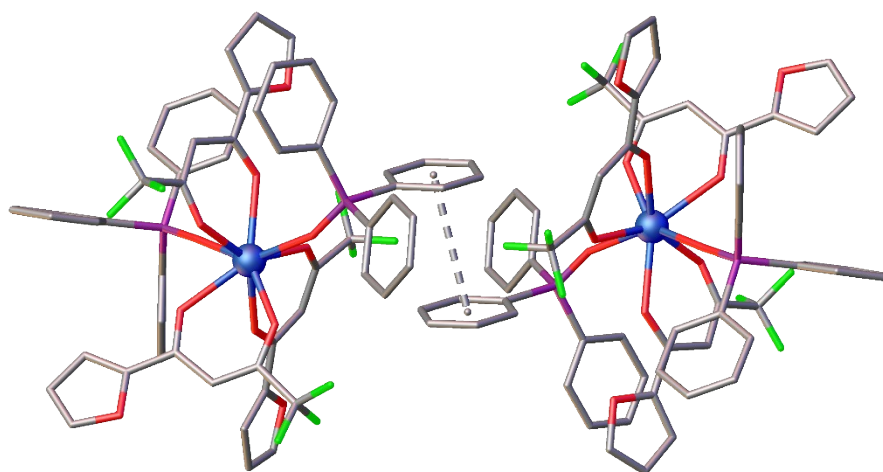


Figure S7. π -stacking (shown in dashed line) in TbL₃. Thermal ellipsoids of atomic displacement, as well as hydrogen atoms, are omitted for clarity. Neighbouring molecule corresponds to symmetry code 1-x, 1-y, 1-z.

Singlet state energy estimation

To estimate the first excited singlet state (S_1) energy, a UV-Vis spectrum of GdL_3 dissolved in MeCN was registered. The 26000 cm^{-1} value was evaluated by a well-known tangent method¹.

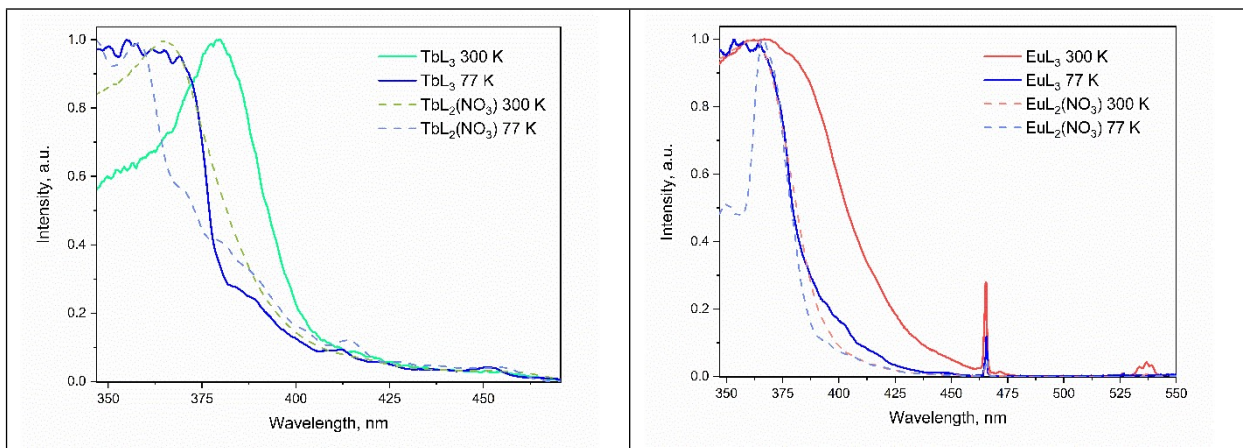


Figure S8. Excitation spectra comparison at different temperatures for complexes TbL_3 , $TbL_2(NO_3)$, EuL_3 , and $EuL_2(NO_3)$.

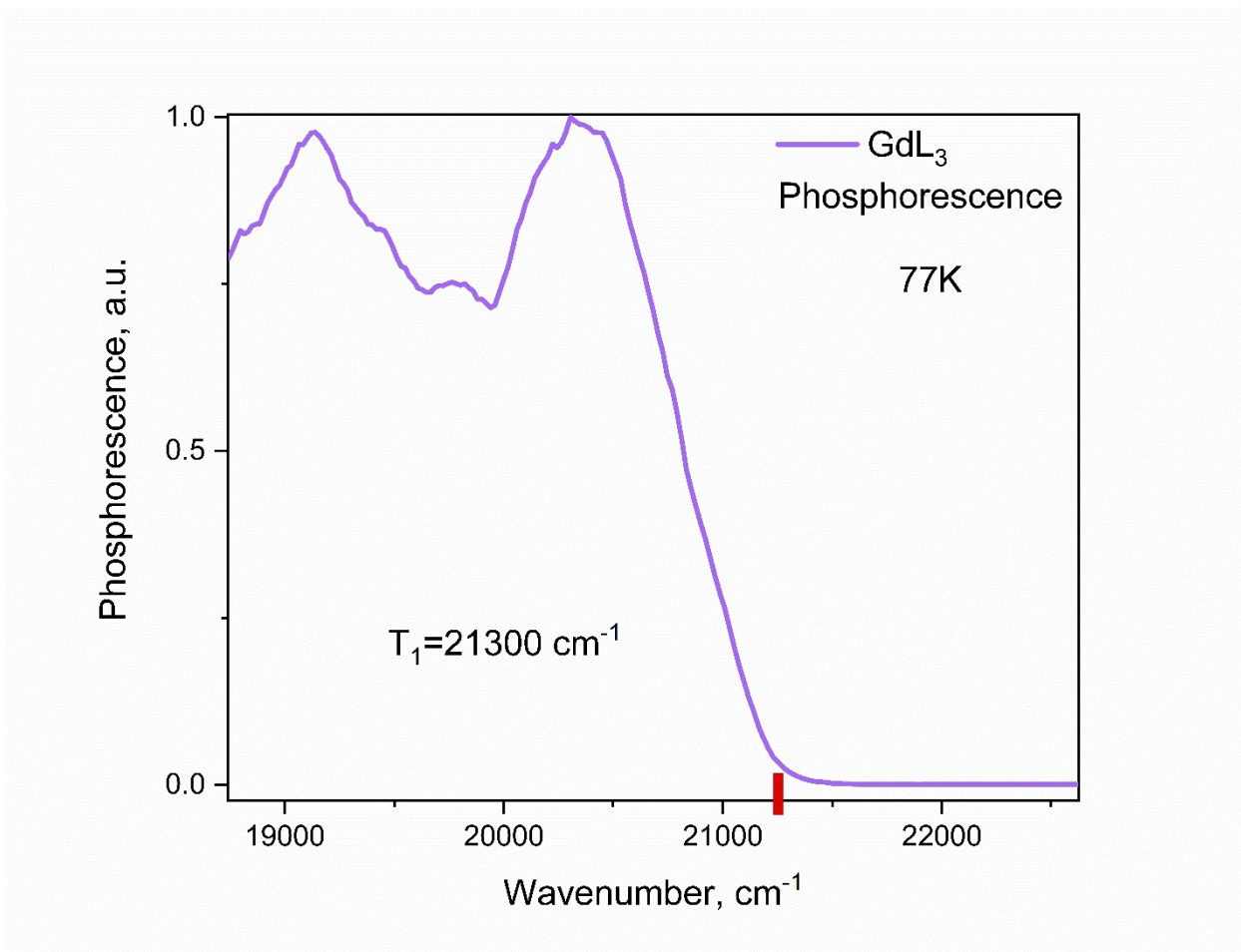


Figure S9. Phosphorescence spectrum of GdL_3 .

Table S4. Electronic transitions of Tb³⁺ and Eu³⁺ ions and the corresponding emission bands observed for Tb/EuL₃ compound.

Eu ³⁺ transitions	Range, nm	Energy, cm ⁻¹
⁵ D ₀ → ⁷ F ₀	578-585	17240
⁵ D ₀ → ⁷ F ₁	590-600	16800
⁵ D ₀ → ⁷ F ₂	610-630	16270
⁵ D ₀ → ⁷ F ₃	645-665	15430
⁵ D ₀ → ⁷ F ₄	685-710	14470
Tb ³⁺ transitions	Range, nm	Energy, cm ⁻¹
⁵ D ₄ → ⁷ F ₆	475-500	20440
⁵ D ₄ → ⁷ F ₅	545-555	18390
⁵ D ₄ → ⁷ F ₄	575-600	17410
⁵ D ₄ → ⁷ F ₃	610-630	16140
⁵ D ₄ → ⁷ F ₂	645-665	15460

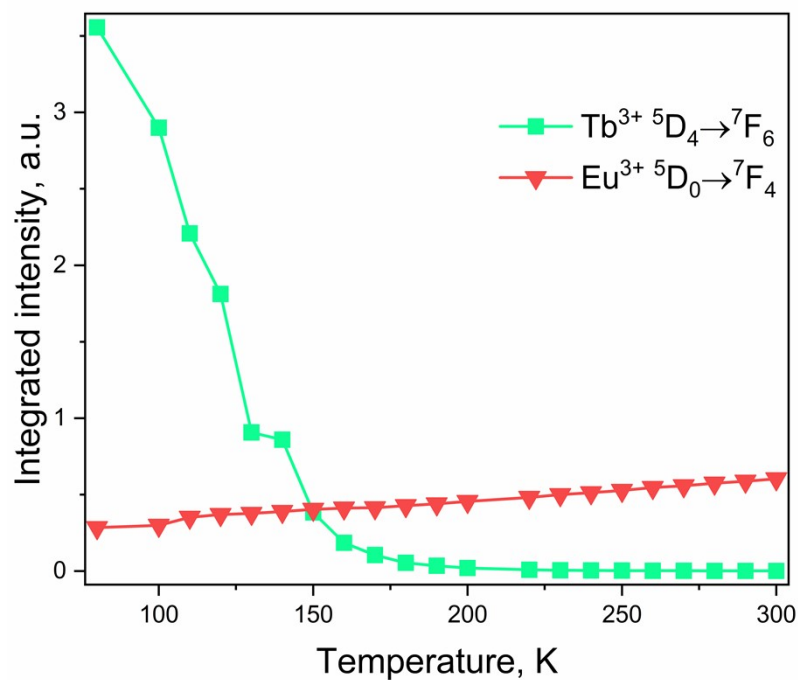


Figure S10. Integrated intensity of spectral bands at different temperatures.

The $\Delta(T)$ dependence can be expressed with accordance to the Boltzmann distribution ²:

$$\Delta = \frac{I_H}{I_L} = B \times \exp\left(-\frac{\Delta E}{kT}\right), \quad (\text{S1})$$

where I_H is the integrated intensity of the emission from the higher-energy excited state, I_L is the integrated intensity of the emission from the lower-energy excited state, ΔE is the energy difference between the thermalized excited states, and k is the Boltzmann constant ($k = 0.695 \text{ cm}^{-1} \text{ K}^{-1}$).

However, a well-known Mott-Seitz model, based on the Boltzmann distribution, is widely used to fit the experimentally obtained Δ values (see Figure 6a)^{2,3}:

$$\Delta(T) = \frac{\Delta_o}{1 + \alpha \times \exp\left(\frac{\Delta E}{kT}\right)}, \quad (\text{S2})$$

where Δ_o – the value of Δ as $T \rightarrow 0 \text{ K}$, α – the ratio of the back energy transfer constant and the sum of the radiative (k_{rad}) and nonradiative (k_{nrad}) relaxation constants.

The adjusted values of fitting parameters are: $\alpha = 10558 \pm 4418$, $\Delta_o = 102432 \pm 2453 \text{ cm}^{-1}$, $R^2 = 0.998$.

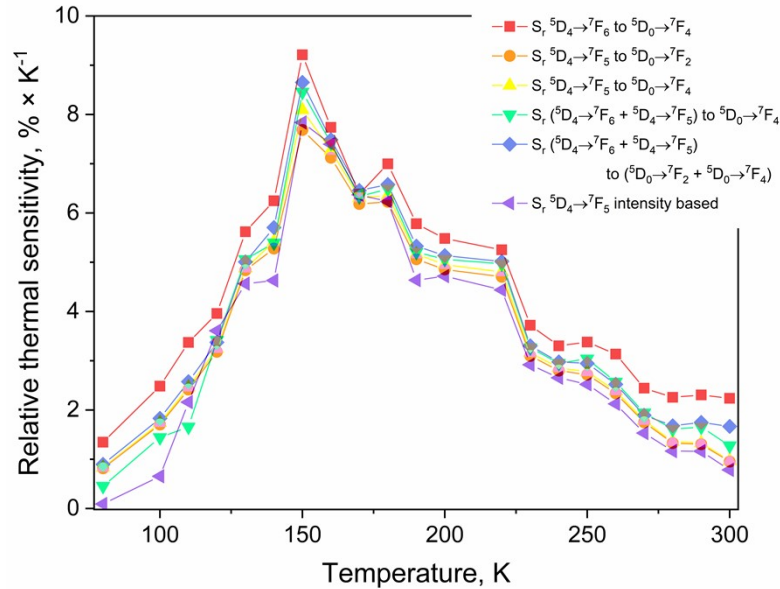


Figure S11. Comparison of relative thermal sensitivity of different spectral bands ratios.

The decays can be fitted by a multiexponential law:

$$I_{th}(t) = \sum_{i=1}^n A_i e^{-\left(\frac{t}{\tau_i}\right)}, \quad (\text{S3})$$

where τ_i and A_i are lifetimes and corresponding amplitudes, respectively.

The measured luminescence decay is determined by:

$$I_{experimental}(t) = \int_0^{\infty} I_{irf}(t') I_{th}(t-t') dt', \quad (S4)$$

where $I_{irf}(t')$ is the instrument response function (IRF), which can be described by an exponential function with the characteristic time $\tau_{irf}=1$ ns.

However, as a rise-time component appears in the decay, the fitting function becomes much more complex as described in section 3.8. The decay curves with a rise-time component can be fitted by the following relations⁴:

$$\begin{cases} C_{Eu^*} = C_1 e^{-k_{Eu}t} + C_2 e^{-(k_{ET} + k_{Tb})t} \\ C_{Tb^*} = C_{Tb^*}^0 e^{-(k_{ET} + k_{Tb})t} \end{cases}, \quad (S5)$$

where:

$$\begin{cases} C_2 = -C_{Tb^*}^0 \frac{k_{ET}}{k_{ET} + k_{Tb} - k_{Eu}} \\ C_1 = C_{Eu^*}^0 - C_2 \end{cases}, \quad (S6)$$

k_{ET} , k_{Tb} and k_{Eu} are rate constants of energy transfer between ions, relaxation from Tb and Eu ions excited states, respectively; $C_{Eu^*}^0$ and $C_{Tb^*}^0$ are populations of corresponding energy levels.

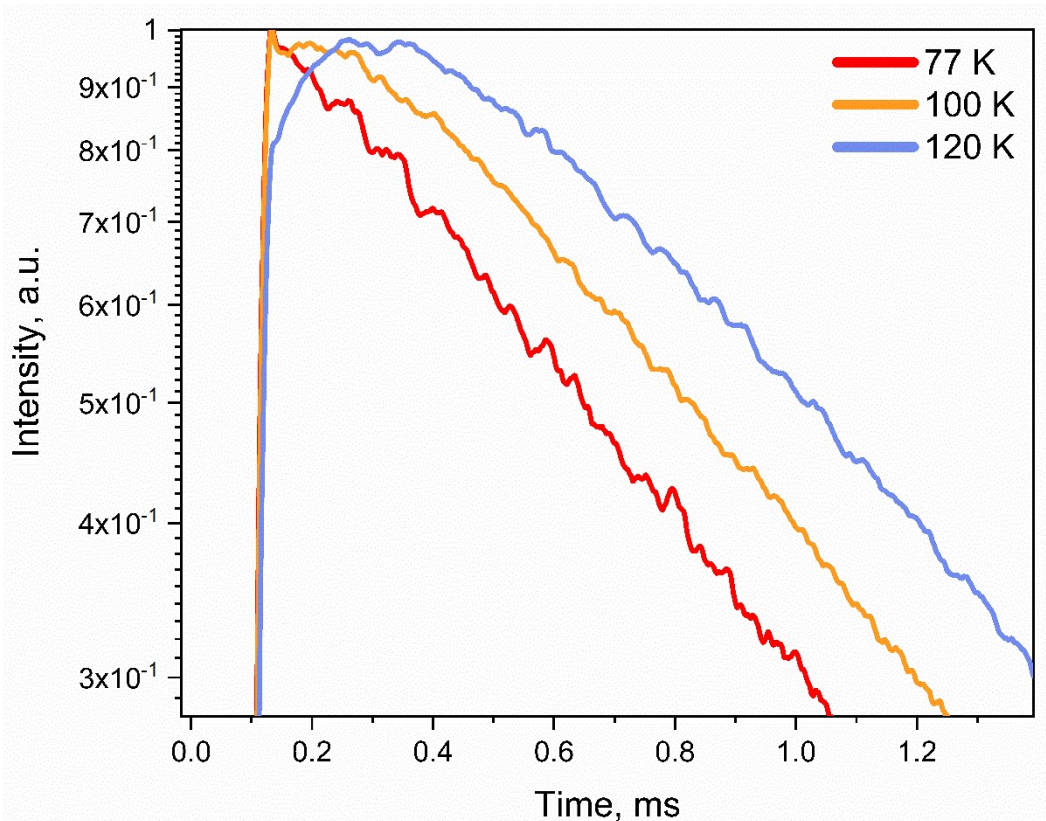


Figure S12. Photoluminescence decays of complex Tb/EuL₃ with registration at 700 nm (Eu³⁺ ⁵D₀ → ⁷F₄) at 77, 100, and 120 K, where the rise-time component appears.

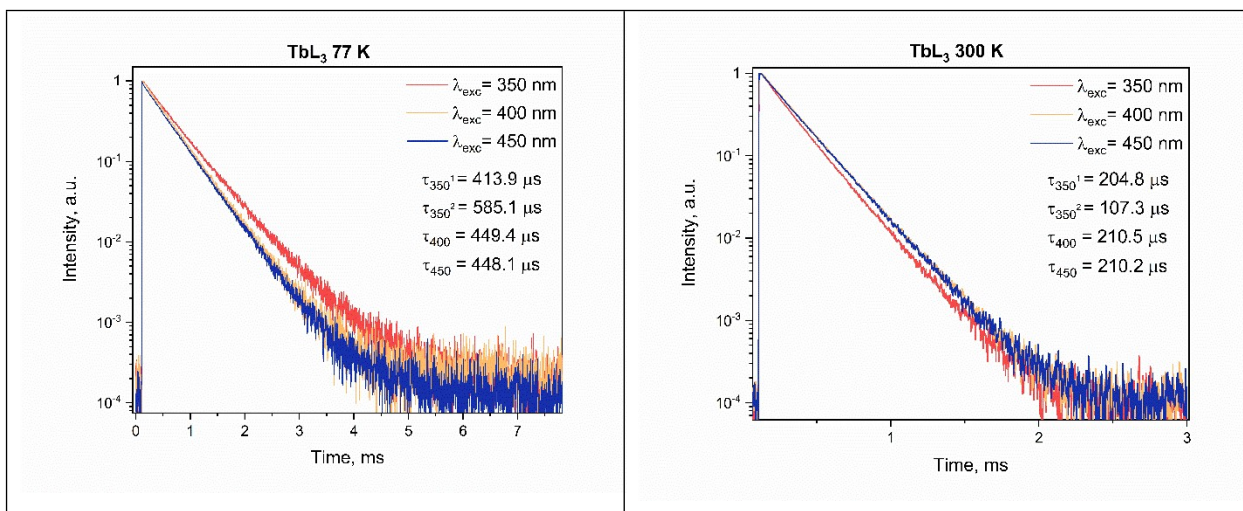


Figure S13. Decays for complex TbL₃ upon different excitation wavelengths (350, 400 and 450 nm) at 77 and 300 K.

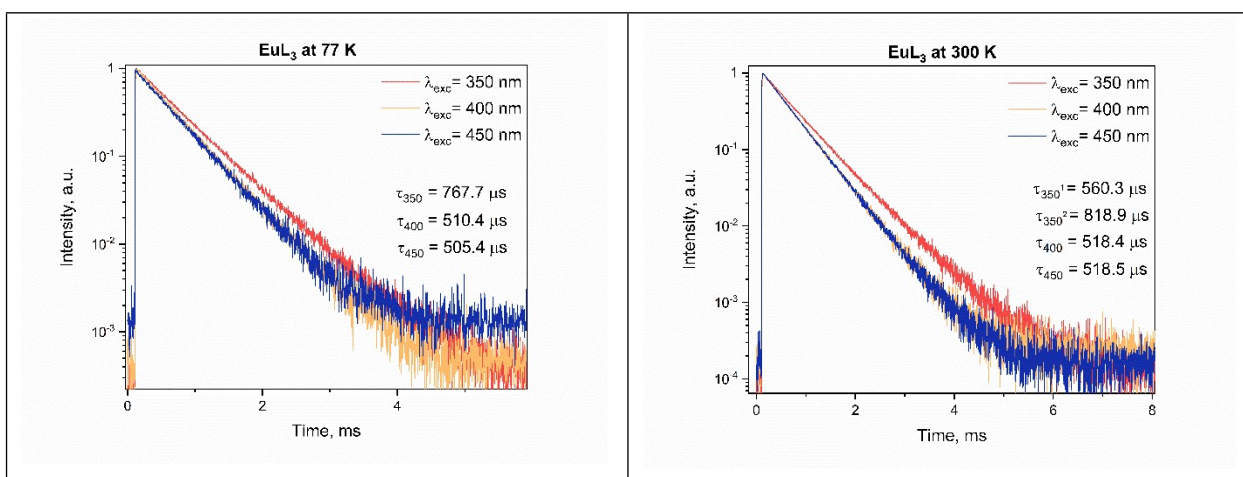


Figure S14. Decays for complex EuL₃ upon different excitation wavelengths (350, 400 and 450 nm) at 77 and 300 K.

The yield $\eta = 1 - \frac{\tau}{\tau_0}$ of the Tb → Eu transfer is 12% (τ is the Tb(⁵D₄) lifetime in the Tb/EuL₃ complex, τ_0 is the lifetime in the pure TbL₃ complex⁵).

The ratio of integrated intensities of electro-dipole (⁵D₀ → ⁷F₂) to magnetic-dipole (⁵D₀ → ⁷F₁) transitions in energy representation is 23.33, which suggests relatively high polarizability and leads to partial resolution of *f-f** transitions.

Signal to noise ratio calculation

To estimate the signal to noise ratio (SNR), we compared the spectra obtained upon the best conditions and spectra used for real-world simulation. The SNR can be calculated as luminescence intensity divided by standard deviation of baseline signal:

$$SNR = \frac{\overline{I_{lum}}}{\sigma_{baseline}}, \quad (S7)$$

where $\overline{I_{lum}}$ is an average maximum intensity of the spectral band, $\sigma_{baseline}$ is the standard deviation of luminescence signal of the baseline close to the considered spectral band.

Thus, we estimated the average SNR for the spectral bands used to calculate Δ , corresponding to $Tb^{3+} {}^5D_4 \rightarrow {}^7F_6$ and $Eu^{3+} {}^5D_0 \rightarrow {}^7F_4$ electronic transitions. The results are shown in Table S5.

Table S5. SNR in Tb/EuL₃ luminescence spectra upon best and “real-world” simulation conditions.

	Ideal conditions	“real-world simulation” dataset
$Tb^{3+} {}^5D_4 \rightarrow {}^7F_6$	235	10
$Eu^{3+} {}^5D_0 \rightarrow {}^7F_4$	295	100

Convolutional neural network

The convolutional neural network architecture depends on the specific task. However, it usually consists of convolutional, pooling and fully-connected (dense) layers.

In a 1D convolutional neural network (CNN), the convolutional layer applies a set of 1D filters (kernels) to the input vector, where each filter performs a convolution operation by sliding along the input vector and computing the dot product between the filter’s weights and the input values. Mathematically, the output of a convolution operation can be defined as⁶:

$$Y(i) = \sum_m X(i+m) \cdot K(m), \quad (S8)$$

where $X(i)$ is the 1D input vector, $K(m)$ is the 1D kernel, and $Y(i)$ is the output feature map.

Max pooling and average pooling are used for down-sampling the feature map. In max pooling, the maximum value within a defined pooling window is selected⁶:

$$Y_{Max}(i) = \max(X(i:i+p)), \quad (S9)$$

where p is the size of the pooling window. The colon sign represents a range of indices. In the context of 1D max pooling, this means that the pooling operation takes a segment of p consecutive elements from the input vector X , starting from position i , and returns the maximum value within that segment.

In average pooling, the average value within the window is calculated⁷:

$$Y_{avg}(i) = \frac{1}{p} \sum_{m=0}^{p-1} X(i+m), \quad (S10)$$

The fully connected layer flattens the pooled 1D feature map into a single vector and connects each input to every output neuron. The output of each neuron z_i is calculated as⁶:

$$z_i = \sum_j w_{ij} \cdot x_j + b_i, \quad (S11)$$

where w_{ij} are the weights, x_j are the inputs from the previous layer, and b_i is the bias term. This layer integrates the extracted features and transfer them to the last unit, which performs the regression task.

A dropout layer was also used before fully-connected layers. Dropout randomly "drops" (sets to zero) a fraction of neurons in the layer during each forward pass, effectively making the network more robust by forcing it to learn redundant representations and preventing reliance on specific neurons^{8,9}.

The loss function, which was the goal to optimize during training (see Figure S15), was commonly used mean absolute error (MAE) function. It is defined as:

$$MAE = \frac{1}{n} \sum_{i=1}^n |y_i - \hat{y}_i|, \quad (S12)$$

where y_i is the true value (label), registered during the experiment, and \hat{y}_i is the predicted value.

The CNN scheme is illustrated in Figure 10. The utilized CNN consisted of 4 convolutional layers with 512,512,256 and 256 feature maps, respectively with kernel size of 15,10,8 and 3, respectively. After second and third convolutional layers max pooling layers were implemented with pooling size 3 and 2, respectively. After fourth convolutional layer, average pooling with pooling size 2 was used. After that, a dropout layer with 0.1 rate was used. Finally, a fully-connected layer with 520 units was used and the last regression unit performed the temperature prediction (see Figure 10 in the main text).

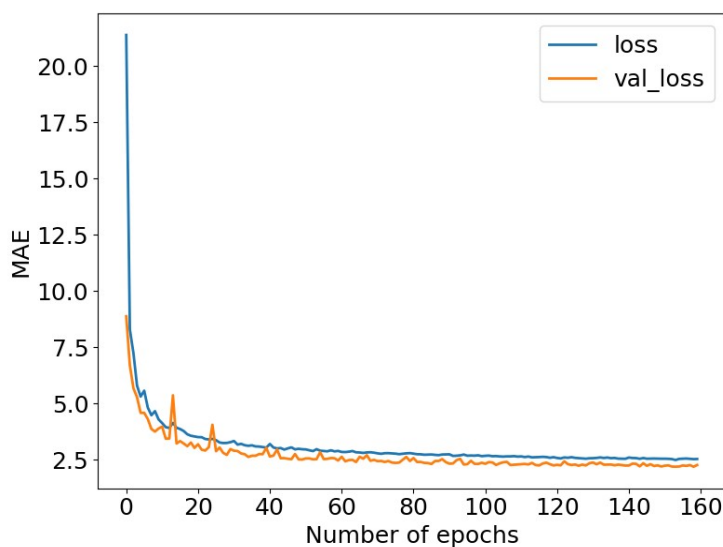


Figure S15. Training and validation loss functions of convolutional neural network.

It should be noted, that the loss function can be slightly higher than the real accuracy of the model, since the dropout layer is used⁹.

- 1 V. Balzani, P. Ceroni and A. Juris, *Photochemistry and photophysics: concepts, research, applications*, Wiley-VCH, Weinheim, 2014.
- 2 M. D. Dramićanin, *Journal of Applied Physics*, 2020, **128**, 040902.
- 3 C. D. S. Brites, S. Balabhadra and L. D. Carlos, *Advanced Optical Materials*, 2019, **7**, 1801239.
- 4 V. E. Gontcharenko, M. A. Kiskin, V. D. Dolzhenko, V. M. Korshunov, I. V. Taydakov and Y. A. Belousov, *Molecules*, 2021, **26**, 2655.
- 5 C. Piguet, J. C. G. Buenzli, G. Bernardinelli, G. Hopfgartner and A. F. Williams, *J. Am. Chem. Soc.*, 1993, **115**, 8197–8206.
- 6 J. Cui, W. Xu, M. Yao, L. Zheng, C. Hu, Z. Zhang and Z. Sun, *Journal of Luminescence*, 2023, **256**, 119637.
- 7 D. Yu, H. Wang, P. Chen and Z. Wei, in *Rough Sets and Knowledge Technology*, eds. D. Miao, W. Pedrycz, D. Ślęzak, G. Peters, Q. Hu and R. Wang, Springer International Publishing, Cham, 2014, vol. 8818, pp. 364–375.
- 8 A. Labach, H. Salehinejad and S. Valaee, DOI:10.48550/ARXIV.1904.13310.
- 9 J. Gu, Z. Wang, J. Kuen, L. Ma, A. Shahroudy, B. Shuai, T. Liu, X. Wang, G. Wang, J. Cai and T. Chen, *Pattern Recognition*, 2018, **77**, 354–377.